Vega-Moreno, J.; Lemus-Santana, A.; Reguera, E.; Andrio, A.; Compañ Moreno, V. (2020). High proton conductivity at low and moderate temperature in a simple family of Prussian blue analogs, divalent transition metal hexacyanocobaltates (III). Electrochimica Acta. 360:1-11. https://doi.org/10.1016/j.electacta.2020.136959

High proton conductivity at low and moderate temperature in a simple family of Prussian blue analogs, divalent transition metal hexacyanocobaltates (III)

J. Vega-Moreno* [1,2], A. A. Lemus-Santana [2], E. Reguera [2], A. Andrio [3], V. Compañ* [4]

[1] CONACyT-Instituto Politécnico Nacional, Centro de Investigación en Ciencia Aplicada y Tecnología Avanzada, Legaria 694, Irrigación, Miguel Hidalgo, CDMX, México
[2] Centro de Investigación en Ciencia Aplicada y Tecnología Avanzada. Unidad Legaría. Instituto Politécnico Nacional. Legaria Núm. 694, Col. Irrigación, Miguel Hidalgo, C.P. 11500 Cd. México
[3] Departamento de Física aplicada. Universitat Jaume I- 12080, Castellón (Spain)
[4] Departamento de Termodinámica Aplicada. Escuela Técnica Superior de Ingenieros Industriales (ETSII). Universidad Politécnica de Valencia, Campus de Vera s/n, 46020-Valencia, Spain.

Abstract

Proton conductivity behavior was studied in a family of hexacyanocobaltates with divalent transition metals (II), HCCMs. The HCCMs, with molecular formula $M_3[Co(CN)_6]_2 \cdot xH_2O$ (where M = Ni, Co, Fe, Mn and Cd), had cubic crystal structures and similar cell parameters. The number of water molecules per formula unit (x) present in each HCCMs was determined from thermogravimetric analysis data. Differences in conductivity values were evaluated by running dielectric impedance experiments. The values of the permittivity and conductivity real and imaginary parts were obtained for each material. The actual conductivity part was analyzed as a temperature and frequency function. Mobilities, diffusivities, and ion charge densities were derived from the electrode polarization model that appropriately fits the loss tangent curves. The measurement conditions for all the samples were relative humidity of 99% and temperature ranging from 25 to 105 °C. The conductivity values obtained for the HCCMs varied from 10^{-4} to 10^{-2} S cm^{-1}. At low temperatures, proton conductivity values for the nickel hexacyanocobaltate (HCCNi) stood out (from 10^{-3} and 10^{-2} S cm^{-1}, at 25 and 45 °C, respectively), followed by Fe, Cd, Co and Mn. In addition to the results stated above, activation energies were determined using the Arrhenius model, where the obtained values were below 21.1 kJ/mol. The proton transport activation energies suggest that the transport through the HCCM porous framework was achieved by the Grotthus mechanism. The diffusivity in the porous framework increased with temperature for all the samples except for HCCNi, following the trend $D_{HCCFe} > D_{HCCMn} > D_{HCCCo} > D_{HCCCd}$. The variability observed between the samples could be related to the ion-binding energies (E_b). These results indicate

that hexacyanocobaltates can be useful as mixed matrix membrane (MMM) fillers, providing excellent conductivity and diffusivity when the medium contains a sufficient amount of ionic components depending on the involved transition metal.

Keywords: Prussian blue analogs, hexacyanocobaltates, conductivity, diffusivity, electrode polarization, polarizability and ionic conduction.

1. Introduction

Hexacyanocobaltates with divalent transition metals, belong to an interesting family of porous coordination polymers that has been the subject matter of studies focused on gas separation and storage [1], catalysis [2], molecular magnets [3] and charge-transport [4,5]. The series of Prussian blue analogs featured in the present research work is formed by the assembling of the hexacyanocobaltate (III) ion, $[Co(CN)_6]^{3-}$ and a divalent metal (M), M = Ni, Co, Fe, Mn, and Cd, resulting in extended 3D solids with $M_3[Co(CN)_6]_2 \cdot xH_2O$ as formula unit. As for the valence of the involved metals, in the resulting coordination polymer, 1/3 of the structural positions of the octahedral building block remains vacant, generating a system of cavities with diameters of about 0.85 nm that are communicated by cylindrical tunnels with diameters of 0.45 nm and related to the N ligand length [6]. On the surface of a given cavity, six M metals with an unsaturated coordination sphere are found. In the as-synthesized solids, these coordination positions are occupied by water molecules, which stabilize additional water molecules through hydrogen bonding interactions until filling the cavity volume. These metal centers at the cavity surface behave as Lewis acid sites, which determine the proton conduction properties of this series of porous solids [6,7]. In this sense, Figure 1 illustrates the porous framework and network of hydrogen bound water molecules. Both coordinated and hydrogen bound water molecules can be removed by soft heating without disrupting the solid framework. This fact explains the potential application of this type of materials for gas separation and storage [1]. This study supports the hypothesis that the formed network of zeolitic and coordinated water molecules and the Lewis acid character of the metal centers found at the cavity surface are appropriate structural features to make possible the proton conduction through the porous framework. Such behavior, would be enhanced when within the tunnels weakly bound water molecules were also located. The latter is possible if the experiment is carried out under high relative humidity. This type of

assisted proton mobility in the interior of coordination polymers was already reported by our research group using tetrabutylammonium hydroxide (guest molecules) to favor a hydrophilic environment within the cavity of Zeolitic Imidazolate Frameworks analogous to ZIF-8 [8]. Similar facilitated proton mobility, i.e., Grotthus mechanism, was described for hexacyanochromates with molecular formula $M_A^{II}[Cr^{III}(CN)_6]_{2/3}\cdot zH_2O$ (where M_A = V, Co) [5]. In the present research, the study of the hexacyanocobaltate family (HCCMs) is aimed at establishing the proton conductivity within isostructural porous materials while showing how this behavior is associated with the nature of the electric field exerted by the assembling cation, which influences the hydrogen network stability.

In this contribution, the proton conductivity in the HCCM family is reported without including ion pairs in the framework, as reported for ZIF materials. [7] In addition, moderate measurement conditions were used: temperatures from 25 to 105 ° C and relative humidity of 99%. In this sense, it is worth mentioning that this is the first study on proton conductivity in a family of divalent transition metal hexacyanocobaltate materials. Finally, based on the electrode polarization (EP) model, mobility, diffusivity and ionic charge density were calculated by modifying the analysis represented by a single Debye relaxation performed in the work by Klein and co-workers.[9] The modification featured in the present work is essentially related to the frequency dependence of complex permittivity, which on this work was expressed in terms of a Cole-Cole function.

Figure 1. Framework of the $M_3[Co(CN)_6]_2\cdot xH_2O$ series for the members that crystallize within a Fm-3m space group (random vacancy distribution). Indicated are the coordinated and hydrogen bonded water molecules. Neighboring cavities remain communicated by a network of sambal tunnels formed by the finite –CN– bond length.

2. Experimental

2.1. Chemical reagents

Potassium hexacyanocobaltate (III) (≥97%), iron (II) sulfate heptahydrate, cobalt (II) sulfate heptahydrate, nickel (II) sulfate heptahydrate, manganese (II) sulfate heptahydrate and cadmium (II) sulfate hydrate were analytical grade purchased from Sigma Aldrich and used as received.

2.2. Synthesis of metal hexacyanocobaltates

Divalent transition metal hexacyanocobaltates(III), with formula $M_3[Co(CN)_6]_2 \cdot xH_2O$ (where M = Ni, Co, Fe, Mn, and Cd), were synthesized at room temperature using the procedure described in previously reported works[10]. Briefly: an aqueous solution of potassium hexacyanocobaltate (III) (0.01 M) was poured into dissolutions of the sulfates of the involved metals. The solutions were stirred magnetically and allowed to stand for a whole week. Subsequently, the resulting products were washed and centrifuged. The pasty solids were allowed to dry at room temperature until constant weight to obtain a powder.

2.3. X-Ray Diffraction

The XRD powder patterns were collected using a D8-ADVANCE diffractometer (Bruker) in reflectance Bragg-Brentano geometry employing Ni-filtered and CuK_α radiation (λ= 1.54187 A˚). These patterns were preliminarily evaluated using the DicVol program. [11] From the reported structural models, the structure corresponding to these powders was refined using the Rietveld method, implemented in the FullProf program. [11]

2.4. Thermogravimetric analysis

A thermogravimetric analyzer from TA Instruments (model 2950) was used for registering thermogravimetric curves for the materials under study. The analysis temperature interval ranged from 25 to 500 °C with a heating rate of 5 °C/min. The experiments were carried out under nitrogen atmosphere using a flux of 60 mL/min. Before starting the thermogravimetric analysis, all the samples were placed in a saturation chamber at 30 °C for a week.

2.5. Impedance spectroscopy measurements.

Impedance spectroscopy measurements were carried out on the HCCM family (HCCNi, HCCCo, HCCFe, HCCMn and HCCCd). The collection of data was made in the 25 - 105°C temperature interval and within the frequency window of $10^{-1} < f < 3x10^7$ Hz at the indicated humidity level in order to obtain the conductivity and diffusivity of the ionic charge carriers. The experiments were performed with amplitude of 100 mV using a Novocontrol broadband dielectric spectrometer (Hundsangen, Germany) integrated with an SR 830 lock-in amplifier with an Alpha dielectric interface. Sample montage and other measurement details are described in the Supporting Information.

3. Results and Discussion

3.1. Structural characterization

According to the results obtained from a Rietveld refinement, the solids under study crystallize with a cubic unit cell, in the Fm-3m space group (and Pm3m, only HCCFe), which is in total agreement with a previously reported crystallographic characterization.[10,12–14] The indexed patterns are available from Figure 1S-a (Supplementary Information). The experimental and fitted patterns and their difference, according to the Rietveld refinement, are shown from Figure 1S-c to 1S-g for all the samples under study (See supporting information).

3.2. Thermogravimetric analysis

Figure 2 shows the thermogravimetric curves (bottom) for the HCCNi, HCCCo and HCCFe samples with their corresponding derivative (top). In general, the HCCM thermograms show similar behavior: overall, a first loss in two steps before 150 °C, related to the evolution of both coordinated and zeolitic water molecules and later to the decomposition of the cyanometallate lattice at a temperature of *c.a.* 270 °C. The hydration degree of the samples, x (water molecules per formula unit), followed the order: HCCNi =17 H_2O > HCCCo = 14 H_2O > HCCCd =13 H_2O > HCCMn = 12 H_2O > HCCFe =11 H_2O, which represents ca. 30% of the total sample weight in terms of their formula unit. Water content has been related to the polarizing power of the metal center since it determines the attractive force between the metal and its coordinated water molecules. In turn, when the coordinated water molecule electron cloud is highly polarized, it leads to a stronger hydrogen bonding interaction with the zeolitic ones, resulting in the formation of a more stable network of weakly bound water molecules within the cavity. This fact explains the dependence of the hydration degree on the metal (M).[10]

Another straight consequence of the metal polarizing power effect becomes evident through the temperature at which the water molecules evacuate the porous structure, which is associated with the H_2O-H_2O and H_2O-framework binding energies. In Figure 2, the derivative curve (d (wt.%) / dT) details the behavior of water molecules inside the solid cavities. In the weight loss below 150 ° C, the first step correlates with the removal of zeolitic water molecules, and the second one with the evacuation of strongly bound water molecules. As it can be seen, at low temperatures (below 90 ° C, approximately), there is a distinctive

metal effect for each composition, where the departure of zeolitic water molecules is sensed indirectly by means of the slope and ending point. The induced effect of the metal polarizing power on the stability of the weakly bound water molecules is clearly distinguished from the amount of zeolitic water molecules found within the cavity and the temperature required for their removal. In the Supporting Information, Figure 2S displays an amplified view of the low temperature region in the TGA and DTG curves. Accordingly, the number of slightly bound water molecules is in HCCNi = 7, in HCCFe = 4, in HCCCo = 2, in HCCCd = 2, and in HCCMn = 1. Once these molecules left the framework, the evacuation of strongly bound molecules started: 11 for Cd, Co and Mn; 10 for Ni and 7 for Fe containing compositions. It is noticeable that within this series of compounds, the lowest number of coordinated water molecules per formula unit and the highest temperature for zeolitic water elimination correspond to iron. Such unique feature within the series could be related to the existence of two non-equivalent structural sites for the iron atom in the framework associated with a non-random vacancy distribution, as assessed by means of Mössbauer spectroscopy [11]. These results suggest that for HCCMs there are factors other than free volume and polarizing power that play a certain role in the amount of water that each composition holds, making it very interesting to determine their conductive behavior. [15]

Figure 2. Thermogram (down) and derivative (upper) of the HCCM samples.

3.3. Impedance spectroscopy

Impedance spectroscopy measurements were carried out on the porous frameworks of divalent transition metal hexacyanocobaltates (III), HCCMs, in the temperatures range between 25 to 105ºC, in order to obtain the conductivity and diffusivity of ionic charge carriers. Both are the most important parameters to characterize and estimate the ionic transport. All the measurements have been done in wet conditions on hydrated samples of HCCMs. The experimental data obtained from the powder samples were analyzed in terms of the complex dielectric permittivity function, $\varepsilon^*(\omega,T)$, and the complex conductivity $\sigma^*(\omega,T) = j\ \omega\ \varepsilon_0\ \varepsilon^*(\omega,T)$, where j is the imaginary unity, ε_0 is the vacuum permittivity and ω the angular frequency of the applied electric field ($\omega=2\pi f$). From the dielectric measurements, the dc-conductivity (σ_{dc}) can be obtained using three different procedures: 1) from the relationship between the complex dielectric permittivity (ε^*) and complex

conductivity; [16] 2) another method to determine the dc-conductivity is by means of the Nyquist diagrams, where the imaginary part is plotted versus the real part of impedance (-Z" vs Z');[17] and 3) the third method to obtain the dc-conductivity is from the Bode diagram.[18,19]. In this work, the conductivities (σ_{dc}) were obtained from the Bode diagrams in the temperature interval ranging from 25 to 105ºC.

Figure 3 shows the Bode diagram for the real part of the conductivity of the samples: HCCNi, HCCCo, HCCFe, HCCMn and HCCCd from a) to e), respectively. Notice that in this plot, the phase angle was also plotted to probe that where the phase angle tends to zero, then the real part of the conductivity is independent of the frequency as is shown by the plateau. This figure reveals that the real part of the conductivity increases with the frequency and tends to a constant value when the phase angle, φ, reaches a maximum tending to zero for each temperature. The change in dc-conductivity (σ_{dc}) of the different HCCMs at different temperatures is observed and can be extracted from the plateau in the high frequency range. Furthermore, the frequency value where the plateau is reached is shifted to higher frequencies by increasing the temperature as a consequence of the thermal activation of proton transport. For example, at 25°C and 99% RH, the dc-conductivity values followed the trend: σ_{HCCNi} (6.87×10^{-3} S cm^{-1}) > σ_{HCCFe} (2.92×10^{-3} S cm^{-1}) > σ_{HCCCo} (0.31×10^{-3} S cm^{-1}) > σ_{HCCCd} (0.1×10^{-3} S cm^{-1}) > σ_{HCCMn} (0.02×10^{-3} S cm^{-1}). Note that the conductivity values obtained at that temperature show a trend that is similar to that displayed by the values of quantity of zeolitic water molecules described before in the thermogravimetric analysis. The parallelism in both trends points out that the participation of guest molecules (in this case zeolitic water) is an important factor in the charge transport in HCCMs. The proton conductivity in HCCMs at 25°C is mainly given by hydrogen bridges stemming from zeolitic water molecules that build a system of interconnected channels inside the framework. The low activation energies, (discussed further) characteristic of the Grotthus mechanism, support this assumption that the proton jumps through hydrogen bridges (usually from water molecules). [20–22]

Another factor that can participate in the charge transport in HCCMs is the coordination environment of metal cations. [12,13] Although HCCFe has a crystalline structure that is similar to that of its analogs [10], it is the only one in the HCCMs family that crystallizes in the Pm3m space group, in which the iron atom can be found in two different coordination

environments: $Fe(NC)_5(H_2O)$ and $Fe(NC)_2(H_2O)_4$. [12] In Table 1S in the Supporting Information, it is worth noting that the dc-conductivity value for HCCFe at room temperature is higher than that of its analogs (except for HCCNi, which has the highest number of zeolitic guests); and with increasing temperature, the conductivity values for HCCFe increase and remain being the highest. Each iron cation in both non-equivalent structural sites can favor the transport of protons slightly differently through the lattice.[5] The observed unique behavior for Ni was ascribed to the strong Lewis acid character for the Ni(2+) ion.

Returning to the Bode diagram (Figure 3), for all the HCCMs, the real part of the conductivity increases with the temperature, keeping the same trend. Only in the case of HCCNi, the conductivity reaches a limit value at 65°C and shows decreased conductivity at higher temperatures. Nonetheless, this limit value is exceptionally high: $1.07x10^{-2}$ S cm^{-1}, an order of magnitude higher than that of its analogs (conductivity in the order of $x10^{-3}$ S cm^{-1}). Such a high conductivity value deserves a detailed analysis.

Precisely, at 65°C ends the removal of the weakly bound water molecules in HCCNi (Figure 2) and represents the last temperature point before the hydrogen bridges disappear. From this mild thermal energy, higher temperatures seem to be transformed into kinetic energy that prevents the stabilization of a water network, i.e. the presence of high relative humidity (99%) does not compensate the lack of hydrogen bridges among guest molecules. This observation confirms the need of interconnected channels, through the system of the mentioned tunnels (Figure 1), to achieve the conductive behavior in HCCMs and also highlights the remarkable heterogeneous character on the surface of the HCCNi cavities, [10] which above 65°C lost 41% of water content (See Figure 1S-b). Presumably, the remaining ten highly polarized associated water molecules form a tightly bound cluster with reduced dimension in comparison with the cluster formed by the eleven water molecules within HCCCo, HCCCd and HCCMn cavities. Table 1S in the Supporting Information summarizes the dc-conductivity values in the temperature interval ranging from 25 to 105 °C. The deviation from the plateau is attributed to the electrode polarization resistance, which results from blocking the charge carriers at the electrodes.

Another particular case is that of the HCCMn bode diagram (see Figure 3-d), where in the real-low frequency region (10–1000 Hz) and real part of the conductivity, a second plateau was observed, where the phase angle also reached a less pronounced second maximum. It is

suggested that the low conductivities associated with the second plateau (4.8 x10^{-4} and 5.3 x10^{-4} S cm^{-1} at 95 and 105 ° C, respectively) are attributed to the formation of new conduction pathways as a consequence of the loss of water molecules in the HCCMn framework. An example of the points stated above is reflected in the decrease in the ionic charge density from 3 x 10^{21} to 1.77 x 10^{21} cm^{-3} and the charge mobility increase from 3.12 to 9.88 m^2 V^{-1} s^{-1} at 95 and 105 ° C, respectively. Table 2S in the Supporting Information presents the values of ionic charge density and charge mobility for HCCMs at different temperatures.

Figure 3-f shows that conductivity in HCCMs follows an Arrhenius behavior, where a linear trend can be described by a single slope through the temperature interval. The thermal activation energy was obtained from the slope of the straight lines shown in each sample. The obtained values displayed the following behavior: E_{act} (HCCCo) = 20.1±0.9 kJ/mol or 0.21±0.09 eV > E_{act} (HCCFe) = 16.5±0.7 kJ/mol or 0.17±0.007 eV > E_{act} (HCCNi) = 16.1±1.1 kJ/mol or 0.16±0.01 eV > E_{act} (HCCMn) = 13.6±0.5 kJ/mol or 0.14±0.005 eV > E_{act} (HCCCd) = 12.8±0.5 kJ/mol or 0.13±0.005 eV, considering the whole temperature interval. These low activation energy values are in agreement with the observed excellent ion mobility. For example: Xia Wang and co-workers [23] reported superprotonic conduction through one-dimensional ordered alkali metal ion chains in a lanthanide-organic framework with conductivities in the order of 10^{-2} S cm^{-1} (at 90 ° C and 90% RH) and ultra-low activation energies of 0.1 eV.

In the light of these results, porous solids of divalent transition metal hexacyanocobaltates with interconnected porous framework may be used as proton conductor materials.

Figure 3. Bode diagrams of the samples: a) HCCNi, b) HCCCo, c) HCCFe, d) HCCMn, e) HCCCd and f) Arrhenius plot for the conductivity of the HCCMs shown in plots a, b, c, d and e.

Figure 4 shows the normalized results with respect to the dc-conductivity (σ_{dc}) and cut-off frequency (f_c). A close inspection of this figure shows that a remarkable coincidence plot was obtained for each sample throughout the studied temperature interval. However, a comparison between the HCCMs allowed to observe that for the HCCCo and HCCFe samples, the recorded isotherms superposed rather well over the reference isotherm, showing that the master curve extends over roughly ten decades. This indicates that charge transport

(protons) is independent of temperature and the assembling cation (Fe or Co) will only affect the mobility and ionic charge density concentration, which implies the existence of a single charge transport mechanism. HCCNi, HCCMn and HCCCd displayed similar behavior, although in such samples, there is a tail indicating that the electrode polarization (EP) has strong temperature dependence in these other samples. The EP is completed at the frequency where the scaling function is not reached, approximately for 4 decades; from 10^{-8} to 10^{-4}, such dependence starts when the ratio $\sigma/\sigma_{dc}<1$. This result has shown that scaling ansatz, [24] is perfectly applicable to such systems, suggesting the existence of an identical thermal activation of charge transport and electrode polarization.

Figure 4. Scaling conductivity curves through the whole temperature interval for the HCCNi, HCCCo, HCCFe, HCCMn and HCCCd samples.

In the experimental assembly, a sample is sandwiched between two circular metallic gold plates with diameter of 10 mm, completely blocking the electrodes. Owing to an EP phenomenon, a suitable analysis should be carried out. Although different EP models have been established to determine the mobility and ionic concentration of charge carriers using impedance spectroscopy measurements, the modified method by Klein and co-workers [9] will be followed in this work. It is based on the Coelho model, [25] where the frequency dependence of complex permittivity is expressed in terms of a Cole-Cole function as

$$\varepsilon^*(\omega) = \varepsilon_\infty + \frac{\Delta\varepsilon_{EP}}{1+(j\omega\tau_{EP})^\alpha} \quad (1)$$

Where $\Delta\varepsilon_{EP} = \varepsilon_{EP} - \varepsilon_\infty$, being ε_{EP} is the dielectric constant when the EP is completely built up and ε_∞ is the static dielectric constant of the sample. The τ_{EP} quantity is the macroscopic EP relaxation time, and it is the time that an ion takes to travel from one electrode to the other through the sample. The exponent α indicates the cumulative process in the system as a consequence of the interactions among charge carriers. If $\alpha << 1$, the interactions are strong, and if $\alpha \leq 1$, the interactions can be considered without influence on the transport process. Finally, j is the imaginary unity ($j = \sqrt{-1}$).

From Eq. (1), the loss tan $\delta = \varepsilon'' / \varepsilon'$ can be obtained as:

$$\tan\delta = \frac{(\omega\tau_{EP})^{\alpha}\sin\left(\frac{\pi\alpha}{2}\right)}{1+2(\omega\tau_{EP})^{\alpha}\cos\left(\frac{\pi\alpha}{2}\right)+\frac{(\omega\tau_{EP})^{2\alpha}}{M}} \quad (2)$$

with $M = \Delta\varepsilon_{EP}/\varepsilon_{\infty} \cong \varepsilon_{EP}/\varepsilon_{\infty}$. If α=1, then Eq. (2) is reduced to the Coelho model, where the EP behavior is represented by a single Debye relaxation, and the expression given in reference [9] for tan δ is recovered:

$$\tan\delta = \frac{(\omega\tau_{EP})}{1+\frac{(\omega\tau_{EP})^{2}}{M}} \quad (3)$$

The quantity *M* is also expressed as $M=L/2L_D$, where L is the sample thickness (i.e. electrode separation when the sample is sandwiched to take the measurements), and L_D is the Debye length defined as $L_D = \sqrt{\frac{\varepsilon_S\varepsilon_0 kT}{q^2 n}}$, where k is the Boltzmann constant, T the absolute temperature, q is the ion charge and n the mobile charge density.

Figure 3S shows the tan δ plots as a frequency function for the series of HCCM materials. In all the cases, a maximum (tan δ_{Max}) can be observed in each curve, which in turn, moves at high frequencies as the temperature increases. The values of the cutoff frequency, fc, frequency that relates the parameters of tan δ_{Max} and frequency with the plateau of the real part of the conductivity in the Bode diagrams (Figure 3) are shown in Table 1S. It should be mentioned that although the determination of the dc-conductivity from the relationship between tan δ_{Max} and the plateau of the real part of conductivity is one of the most widely used methods, it has certain limitations since it is a graphical method. On the other hand, the adjustment of tan δ with models such as Cole-Cole and Debye provide greater certainty in obtaining useful parameters for the determination of the dc-conductivity, mobility, diffusion coefficients and free charge density, among others.

Eq. (2) has been used to fit the tan δ experimental data to provide the estimation of the M, τ_{EP} and α parameters. In Tables 1a and 1b, we shown the values of these parameters, which were calculated using the Cole-Cole and Debye models, respectively, for three temperatures 25, 65 and 105°C, respectively.

In Figure 5, the fitting of Tan δ as a function of the frequency for the HCCCo, HCCFe, HCCMn and HCCCd materials at 65 ºC can be seen.

Table 1a. Parameters M, τ_{EP} and α of Eq. (2) using the Cole-Cole model for some temperatures, from fitting the experimental data of tan δ.

Sample	**T=25°C**			**T=65°C**			**T=105°C**		
	M	**τ_{EP} x10^5 /s**	**α**	**M**	**τ_{EP} x10^5 /s**	**α**	**M**	**τ_{EP} x10^5 /s**	**α**
HCCNi	10642	1.94	0.90	11000	2.1	0.90	2500	0.50	0.92
HCCCo	3800	26.00	0.93	3100	5.5	0.96	2000	1.80	1
HCCFe	1550	2.50	0.83	1400	1.0	0.81	700	0.90	0.75
HCCMn	748	12.70	0.82	405	9.5	0.76	165	1.70	0.75
HCCCd	3600	37.50	0.90	8200	2.6	0.98	13900	0.31	1

Table 1b. Parameters M and τ_{EP} for the Debye model, which was obtained from considering α=1 in Eq. (6) for some temperatures, from fitting the experimental data for tan δ.

Sample	**T=25°C**			**T=65°C**			**T=105°C**		
	M	**τ_{EP} x10^5 /s**	**α**	**M**	**τ_{EP} x10^5 /s**	**α**	**M**	**τ_{EP} x10^5 /s**	**α**
HCCNi	31200	1.80	1	550000	2.00	1	-	-	1
HCCCo	6500	23.00	1	4620	0.93	1	4360	0.38	1
HCCFe	8000	1.70	1	8200	0.90	1	7500	0.65	1
HCCMn	3250	9.60	1	410	9.30	1	990	0.90	1
HCCCd	9100	32.40	1	9300	2.50	1	13900	0.31	1

A close inspection of Table 1 shows that the relaxation time τ_{EP} and the parameter M depend on the temperature. In general, both parameters diminish with temperature increments. Therefore, for all the samples and temperatures, the values of the M parameter using the Cole-Cole model are lower than those obtained with the Debye model while for τ_{EP}, the opposite happens.

Figure 5. Tan δ as a function of the frequency at 65 ºC for HCCCo, HCCCd, HCCMn and HCCFe. The solid lines indicate the convolution of Eq. (2) at the peak of tan δ at higher frequencies.

The curves shown in Figure 5 display peaks corresponding to the maxima in Tan δ (Eq. (2)) and are associated with the plateau of the real part of the conductivity observed in the Bode

diagrams displayed in Figure 3. According to such figures, the conduction peaks in Tan δ are reached at:

$$\omega_{\max}^{\tan\delta} = \frac{M^{\frac{1}{2\alpha}}}{\tau_{EP}} \tag{6}$$

and their corresponding frequency values are related to the parameters M, τ_{EP} and α through Eq. (6), where τ_{EP} is the relaxation time when the electrode polarization is completely built up, and it is associated with the dc-conductivity and permittivity at EP by Eq. (7) [9,26,27]:

$$\tau_{EP} = \frac{\varepsilon_{EP}\varepsilon_0}{\sigma_{dc}} \tag{7}$$

The parameters τ_{EP} and ε_{EP} are related to M trough the expressions $\tau_{EP} = M\tau$ and $\varepsilon_{EP} = M\varepsilon_S$, where τ is the dielectric relaxation time and ε_s is the static permittivity of the material. By taking into account Eq. (6), the following equation is obtained:

$$\tau_{EP} = \tau_m M^{\frac{1}{2\alpha}} \tag{8}$$

And the total relaxation time of the sample, τ, will be ascribed to τ_{EP} and τ_m through Eq. (9):

$$\tau = \frac{\tau_m^2}{\tau_{EP}} = \frac{\tau_m}{M^{\frac{1}{2\alpha}}} \tag{9}$$

3.3.1. Mobility, diffusivity and free charge density

The ionic charge density and ion mobility were obtained from measurements of Tan δ. Considering that cation and anion have approximately the same mobility, μ, and neglecting ion-ion interactions, the conductivity, σ_{dc} ,can be expressed in terms of n and μ as[17,27–29]:

$$\sigma_{dc} = nq\mu \tag{10}$$

where n is the total ion concentration, q is the elementary charge and μ is the ionic mobility. Using the equations of τ_{EP} and ε_{EP} in terms of M together with Eqs. (7-10), the mobility is determined as:

$$\mu = \frac{qL^2}{4M\tau_{EP}kT} \tag{11}$$

and then, by taking into account the Einstein ratio for ion diffusivity together with Eqs. (6-11), the diffusion coefficient is calculated as:

$$D = \frac{L^2}{4M\tau_{EP}} \tag{12}$$

Other expressions can be obtained considering Eq.(9). By means of this expression, the following are also obtained:

$$D = \frac{L^2}{4M^{3/2}\tau_m} \tag{13}$$

and

$$D = \frac{L^2}{4M^2\tau} \tag{14}$$

Whatever of Eqs. (12-14) allows to determine the ion diffusivity in terms of parameters M, τ_{EP}, τ_m, τ and L.

Finally, the ionic charge density was obtained from conductivity and diffusivity values as:

$$n = \frac{\sigma_{dc}kT}{Dq^2} \tag{15}$$

The diffusivity values (*D*) obtained using Eq. (13) are shown in Figure 6-a as a function of the temperature. From this figure, a diffusivity effect similar to the one observed in conductivity, except for the HCCNi sample (see Arrhenius plot in Figure 6-a), is appreciated independently of the model used to calculate the diffusivities. Notice that the HCCNi sample presents a behavior pattern that is opposite to the one displayed by the other samples. In general, diffusivity increases with temperature increments, except for the HCCNi sample, where a decrease is observed at least at the temperatures between 25 and 35ºC.

Figure 6. Arrhenius diagram for a) diffusion coefficient and b) charge mobility obtained from the Cole-Cole model.

A close inspection of the variation of the values represented in the activation plot in Figure 6-a suggests that excellent ion diffusivity can be obtained with the studied HCCMs. The diffusivity rises as the temperature increases for all the samples, except for HCCNi, following the trend $D_{HCCFe} > D_{HCCMn} > D_{HCCCo} > D_{HCCCd}$. The variability observed with temperature among the samples could be related to the ion binding energies (E_b). Following Eisemberg, [30] the energy necessary to separate contact ion pairs on the samples was calculated using Eq. (16):

$$E_b = \frac{-q^2}{4\pi\varepsilon_\infty\varepsilon_0 r} \tag{16}$$

where *r* represents the separation between centers of contact ions. Supposing that the ionic radio is compressed between 3 and 4 Å, the binding energy is dependent on static permittivity. Table 1S in the Supporting Information shows the theoretical and experimental values of the static permittivity, ε_s, obtained for each sample.

A close inspection of these values shows that the binding energy will vary with temperature. For example, for the HCCCo sample, this value varies from 4.76 to 5.5 kJ/mol (from 25 to 105ºC, respectively). For HCCCd, the variation was from 9.63 to 10.70 kJ/mol. In the case of HCCMn, it results from 10.7 to 7.1 kJ/mol. The values changed from 8.4 to 3.4 kJ/mol for HCCFe, and from 9.6 to 14 kJ/mol for the HCCNi sample. From such results, it can be concluded that for the HCCCo, HCCCd and HCCNi samples, the binding energies increase with temperature increments and the opposite happens with the HCCMn and HCCFe samples, respectively. From the calculated values for binding energy, the stabilization energy E_s can be calculated using the values obtained for the activation energy by means of $E_s = E_a - E_b$. [9] The values resulting from varying the temperature are in agreement with the ion pair binding energy between 15.3 and 14.5 kJ/mol for HCCCo, 3.2-2.1 kJ/mol for HCCCd, 3-6.5 kJ/mol for HCCMn, 8.1-13.1 kJ/mol for HCCFe and from 6.5 to 2.1 kJ/mol in the case of HCCNi.

The comparison between them reveals that a decrease in the ion binding energies (E_b) and stabilization energies (E_s) produces a decrease in the diffusion coefficient around one or two orders of magnitude depending on the temperature and assembling transition metal in the HCCMs. From the diffusivity values calculated from Eq. (13), it can be concluded that the

diffusivity of HCCNi is lower than of the other samples. The diffusivity of HCCo is close to the one of HCCCd and both are lower than those of HCCFe and HCCMn, respectively. For example, at 65ºC, the diffusivities are 5.97×10^{-6}, $2.54x10^{-6}$, 8.5×10^{-7}, 7.6×10^{-7} and 7.3×10^{-7} $cm^2\ s^{-1}$ for HCCFe, HCCMn, HCCNi, HCCo, and HCCCd, respectively. The ion mobility calculated from the electrode polarization model through Eq. (11) is represented in Figure 6-b. The obtained values follow the same evolution as the diffusivity plotted in Figure 6-a.

A close inspection of Figure 6-b shows that the mobility of HCCMs increases with temperature increments, and is approximately an order of magnitude greater when the sample is HCCCo, HCCFe, and HCCMn with respect to HCCCd and HCCNi. In particular, the mobility of the HCCNi sample (see inset of figure 6-b) exhibits atypical behavior, compared to its analog HCCMs: when the temperature increases from 25 to 65 °C, a slight decrease in mobility is observed and subsequently, from 65 to 105 °C a considerable increase in three orders of magnitude. Another particular behavior exhibited by the HCCNi is the increase in the density of the charge carriers in an order of magnitude, within the range of 25 to 65 °C and subsequently, starting at 65 °C, the density of the carriers of charge slightly reduced (see Figure 5S). Accordingly, the behavior of charge carrier density and ion mobility in the HCCNi sample can be explained in terms of the behavior of the metal cation as Lewis acid and its polarizing power. Whereas, on the surface of the lattice cavity HCCMs, six M metals are found with an unsaturated coordination sphere, the charge density of the metal centers, polarizing a first sphere of water molecules (water molecules coordinated), which in turn stabilize the addition water molecules (zeolitic water molecules) through hydrogen bonding interactions to fill the cavity volume. [10] Note that, the Ni metal cation (compared to the metal cations of Fe, Co, Mn and Cd), have a greater behavior as Lewis acid and a greater polarizing power. [10,31] With the increase in temperature from 25 to 65 °C, water molecules weakly bound to Ni metal (polarized and captive inside the cavity) begin to vibrate more rapidly, resulting in an increase in the density of charge carriers (in addition to this, slightly reduces mobility). Subsequently, after 65 °C, after the loss of zeolitic water molecules (see TGA analysis in section 3.2), the density of charge carriers reduces, giving way to increased mobility as can be seen in the inset of Figure 6-b. The increased mobility at temperatures above 65 °C can be explained by the participation of water molecules (coordinated) and metal

sites (which function as Lewis acid sites), for the formation of pathways that promote the transport of charge through the framework.

Another possible explanation is the potential barrier that the anion must overcome to move from one ion pair to the next. If the amount of anions increases, the distance between neighboring ion pairs decreases and their Coulomb potential barrier increasingly overlaps, decreasing the energy to produce a jump and after following the hopping mechanism. A similar mechanism has been proposed by other researchers to explain the increase in conductivity of different polymer salt electrolytes and in PPO/salt systems.[32–34].

When the values of the inverse Debye length can be obtained from the peaks of the loss tangent, the values of static permittivity, ε_s, can be estimated. Eq. (17) provides an indirect method to calculate these values. This method can be compared with the equation by Anatoly Serghei, [35] where the permittivity can be expressed as a function of the f_{ON} and f_{Max} values found from the curves of double logarithmic plot of σ" versus frequency, as stated by Serghei:

$$\varepsilon_s = \frac{\sigma_{dc}}{2\pi\varepsilon_0}\frac{f_{Max}}{f_{ON}^2} \tag{17}$$

where f_{ON} is the onset frequency, where the electrode polarization starts to develop and f_{MAX} is the frequency, where the full development of electrode polarization has been built.
Figure 4S shows the curves of double logarithmic plot of σ" versus frequency in the whole temperature interval considered for HCCCo, HCCCd, HCCMn and HCCFe, respectively. From this figure, for each sample at each temperature, the frequency values of the onset (f_{ON}) and full development of electrode polarization (f_{MAX}) were established, respectively, which allowed the computation of the static permittivity following Eq. (17). The mean values obtained following the two procedures are gathered in Table 1S as theoretical ε_s. Also, for comparison purposes, the values observed from the experimental plots of ε' versus frequency for all the samples were tabulated as experimental ε_s. A comparison between both results reveals the excellent agreement between the static permittivity values obtained theoretically following Eq. (17) with respect to the experimental ones. A close inspection of these results indicates that ε_s decreases when the temperature increases for the HCCCo, HCCCd and HCCNi samples. The opposite is observed for the other samples (HCCCFe and HCCMn).

Finally, the comparison between the permittivity of the samples shows that the values displayed by HCCCo and HCCFe are higher than those of HCCNi.

Once calculated the values for the binding energy and stabilization energy E_s in previous sections, the activation energy for conductive behavior can be analyzed as the sum of both contributions by the relationship of $E_s + E_b = E_a$. In accordance, at each temperature point it is possible to ponderate the contribution of the assembling ion (as E_b) and the contribution of water network (E_s) for the conductive behavior in HCCMs. An example for each composition at 25°C and 105° C is illustrated in Figure 6S.

Figure 7 shows a description of the correspondence between the time/frequency and temperature for the conductivity using the scaling ansatz, [24] where log (σ''/σ_{dc}) scaling with log (f/f_c), being f_c the frequency marking the onset of the dc-conductivity. This result shows that the scaling function is also perfectly applicable to our samples, and the straight-line displayed between the minimum and the maximum of the plot (i.e. the frequency at which the electrode polarization starts and the frequency where the EP has been completely built up, having practically the same slope.

Figure 7. Master curve of the normalized plots with respect to the imaginary part of the conductivity of the samples plotted in Figure 4S.

The experimental measurements obtained for the permittivity (ε' and ε") and conductivity (σ' and σ") collapsed onto a single chart when normalized. All the charts collapsed into one if scaled with respect to f_c. This suggests an identical thermal activation of charge transport and electrode polarization.

Conclusions

From the standard chemical precipitation method, transition metal hexacyanocobaltates (III), $M_3[Co(CN)_6]_2 \cdot xH_2O$ (where M = Ni, Co, Fe, Mn, and Cd), were obtained as powders. Each solid reached a different hydration degree under saturation. The thermogravimetric analysis showed two steps, in overall, for each composition of HCCMs to evacuate the large amount of hydrogen bound guest molecules. In this family of porous materials, the removal of lightly bound water molecules starts from very low temperatures (25°C) and achieves total dehydration (ca. 30% in weight) at around 140°C.

Nonetheless, the behavior of the TG curves differs significantly, which suggests that it does not matter if the family has similar structure and pore volume, the water networks flow through tracks determined by each specific material, which is particularly determined by the nature of the involved metal.

Samples of HCCMs were evaluated by means of dielectric impedance spectroscopy and conductivity values were determined. The values of the proton conductivity obtained for HCCNi and HCCFe (at 99% RH and room temperature) are in the order of 10^{-3} S cm^{-1} while HCCCo, HCCMn and HCCCd presented values in the order of 10^{-4} S cm^{-1}. It should be mentioned that approximately from 45 and 95 ºC, HCCNi and HCCFe, respectively, presented proton conductivities in the order of 10^{-2} S cm^{-1}. For the studied HCCMs family, HCCNi presents the highest conductivity value at 99% RH and 25°C while HCCFe displayed the highest conductivity value at 99% RH and 105°C.

According to the activation energies derived from the proton conductivity (<21.1 kJ / mol), the proton conduction processes in the HCCMs occur according to the Grotthuss mechanism. The diffusivity in the HCCNi sample is lower than the one for the other samples and at 65ºC, the diffusivities are 7.6×10^{-5}, 7.3×10^{-5}, 5.97×10^{-6}, $1.64\text{x}10^{-6}$ and 4.2×10^{-8} cm^2/s for HCCo, HCCCd, HCCFe, HCCMn and HCCNi, respectively. The unique behavior displayed by Ni, from the metals herein considered, is related to its stronger acidic character in terms of Lewis acids. In each composition and temperature points, the activation energies are the sum of Eb and Es, which were clearly distinguished inside the cavities of HCCMs.

Finally, a comparison between the static permittivity values obtained theoretically following the Anatoly Serghei formula, Eq. (17), and the experimental ones, showed that they were in excellent agreement.

Acknowledgments

This research has been supported by the ENE/2015-69203-R project, granted by the Ministerio de Economía y Competitividad (MINECO), Spain, Also authors are grateful to UNAM-DGAPA-PAPIIT projects IG-100185, and IG-114818.

This study was partially supported by the CONACyT (Mexico) projects 2013-05-231461 and CB-2014-01-235840.

The authors appreciate the access to the experimental facility of the National Laboratory for Energy Conversion and Storage (CONACyT) to carry out the experimental study.

Bibliography

[1] L. Reguera, J. Balmaseda, L.F. Del Castillo, E. Reguera, Hydrogen storage in porous cyanometalates: role of the exchangeable alkali metal, J. Phys. Chem. C. 112 (2008) 5589–5597. https://doi.org/10.1021/jp7117339.

[2] Z.Y. Liu, G.T. Fu, L. Zhang, X.Y. Yang, Z.Q. Liu, D.M. Sun, L. Xu, Y.W. Tang, PdCo/Pd-Hexacyanocobaltate Hybrid Nanoflowers: Cyanogel-Bridged One-Pot Synthesis and Their Enhanced Catalytic Performance, Sci. Rep. 6 (2016) 1–10. https://doi.org/10.1038/srep32402.

[3] X.Y. Liu, L.Q. Duan, Q. Wei, S.P. Chen, Two cyanide-bridged compounds composed of Schiff base-manganese(III) building block with dicyanamido and hexacyanocobaltate(III) as ligands: Crystal structure, thermostability and magnetic property, Inorganica Chim. Acta. 423 (2014) 462–468. https://doi.org/10.1016/j.ica.2014.09.009.

[4] K. Ono, M. Ishizaki, K. Kanaizuka, T. Togashi, T. Yamada, H. Kitagawa, M. Kurihara, Grain-Boundary-Free Super-Proton Conduction of a Solution-Processed Prussian-Blue Nanoparticle Film, Angew. Chemie Int. Ed. 56 (2017) 5531–5535. https://doi.org/10.1002/anie.201701759.

[5] S.I. Ohkoshi, K. Nakagawa, K. Tomono, K. Imoto, Y. Tsunobuchi, H. Tokoro, High proton conductivity in prussian blue analogues and the interference effect by magnetic ordering, J. Am. Chem. Soc. 132 (2010) 6620–6621. https://doi.org/10.1021/ja100385f.

[6] A. Simonov, T. De Baerdemaeker, H.L.B. Boström, M.L. Ríos Gómez, H.J. Gray, D. Chernyshov, A. Bosak, H.B. Bürgi, A.L. Goodwin, Hidden diversity of vacancy networks in Prussian blue analogues, Nature. 578 (2020) 256–260. https://doi.org/10.1038/s41586-020-1980-y.

[7] A. Jaffe, J.R. Long, Ordered absences observed in porous framework materials, Nature. 578 (2020) 222–223. https://doi.org/10.1038/d41586-020-00329-5.

[8] J. Vega, A. Andrio, A.A. Lemus, L.F. del Castillo, V. Compañ, Conductivity study of Zeolitic Imidazolate Frameworks, Tetrabutylammonium hydroxide doped with Zeolitic Imidazolate Frameworks, and mixed matrix membranes of Polyetherimide/Tetrabutylammonium hydroxide doped with Zeolitic Imidazolate Frameworks for proton conducting applications, Electrochim. Acta. 258 (2017) 153–166. https://doi.org/10.1016/j.electacta.2017.10.095.

[9] R.J. Klein, S. Zhang, S. Dou, B.H. Jones, R.H. Colby, J. Runt, Modeling electrode polarization in dielectric spectroscopy: Ion mobility and mobile ion concentration of single-ion polymer electrolytes, J. Chem. Phys. 124 (2006) 144903. https://doi.org/10.1063/1.2186638.

[10] J. Roque, E. Reguera, J. Balmaseda, J. Rodríguez-Hernández, L. Reguera, L.F. del Castillo, Porous hexacyanocobaltates(III): Role of the metal on the framework properties, Microporous Mesoporous Mater. 103 (2007) 57–71. https://doi.org/10.1016/j.micromeso.2007.01.030.

[11] J. Rodríguez-Carvajal, Introduction to the Program FULLPROF: Refinement of Crystal and Magnetic Structures from Powder and Single Crystal Data, n.d.

[12] E. Reguera, H. Yee-Madeira, S. Demeshko, G. Eckold, J. Jimenez-Gallegos, Nature of the observed asymmetry in mossbauer spectra of iron (2+) hexacyanometallates (III), Zeitschrift Fur Phys. Chemie. 223 (2009) 701–711. https://doi.org/10.1524/zpch.2009.5455.

[13] S. Adak, L.L. Daemen, M. Hartl, D. Williams, J. Summerhill, H. Nakotte, Thermal expansion in 3d-metal Prussian Blue Analogs - A survey study, J. Solid State Chem. 184 (2011) 2854–2861. https://doi.org/10.1016/j.jssc.2011.08.030.

[14] G.M. A. Ferrari, M.E. Tani, Struttura di alcuni cobaltiesacianuri di metalli bivalenti, Gazz. Chim. Ital. 89 (1959) 2512–2525.

[15] A. Alowasheeir, S. Tominaka, Y. Ide, Y. Yamauchi, Y. Matsushita, Two-dimensional cyano-bridged coordination polymer of Mn(H2O)2[Ni(CN)4]: Structural analysis and proton conductivity measurements upon dehydration and rehydration, CrystEngComm. 20 (2018) 6713–6720. https://doi.org/10.1039/c8ce01400k.

[16] I. Fuentes, A. Andrio, F. Teixidor, C. Viñas, V. Compañ, Enhanced conductivity of sodium versus lithium salts measured by impedance spectroscopy. Sodium cobaltacarboranes as electrolytes of choice, Phys. Chem. Chem. Phys. 19 (2017) 15177–15186. https://doi.org/10.1039/c7cp02526b.

[17] T.M.W.J. Bandara, M.A.K.L. Dissanayake, I. Albinsson, B.E. Mellander, Mobile charge carrier concentration and mobility of a polymer electrolyte containing PEO and Pr4N + I- using electrical and dielectric measurements, Solid State Ionics. 189 (2011) 63–68. https://doi.org/10.1016/j.ssi.2011.03.004.

[18] A. García-Bernabé, A. Rivera, A. Granados, S. V. Luis, V. Compañ, Ionic transport on composite polymers containing covalently attached and absorbed ionic liquid fragments, Electrochim. Acta. 213 (2016) 887–897. https://doi.org/10.1016/j.electacta.2016.08.018.

[19] V. Compañ, S. Molla, E. García Verdugo, S. V. Luis, M.I. Burguete, Synthesis and characterization of the conductivity and polarization processes in supported ionic liquid-like phases (SILLPs), J. Non. Cryst. Solids. 358 (2012) 1228–1237. https://doi.org/10.1016/j.jnoncrysol.2012.02.028.

[20] N. Agmon, The Grotthuss mechanism, Chem. Phys. Lett. 244 (1995) 456–462. https://doi.org/10.1016/0009-2614(95)00905-J.

[21] T. Grancha, J. Ferrando-Soria, J. Cano, P. Amorós, B. Seoane, J. Gascon, M. Bazaga-García, E.R. Losilla, A. Cabeza, D. Armentano, E. Pardo, Insights into the Dynamics of Grotthuss Mechanism in a Proton-Conducting Chiral bioMOF, Chem. Mater. 28 (2016) 4608–4615. https://doi.org/10.1021/acs.chemmater.6b01286.

[22] J.M. Taylor, K.W. Dawson, G.K.H. Shimizu, A water-stable metal-organic

framework with highly acidic pores for proton-conducting applications, J. Am. Chem. Soc. 135 (2013) 1193–1196. https://doi.org/10.1021/ja310435e.

[23] X. Meng, H.N. Wang, S.Y. Song, H.J. Zhang, Proton-conducting crystalline porous materials, Chem. Soc. Rev. 46 (2017) 464–480. https://doi.org/10.1039/c6cs00528d.

[24] R. Murugaraj, Ac conductivity and its scaling behavior in borate and bismuthate glasses, J. Mater. Sci. 42 (2007) 10065–10073. https://doi.org/10.1007/s10853-007-2052-5.

[25] R. Coelho, On the static permittivity of dipolar and conductive media - an educational approach, J. Non. Cryst. Solids. 131–133 (1991) 1136–1139. https://doi.org/10.1016/0022-3093(91)90740-W.

[26] U.H. Choi, A. Mittal, T.L. Price, H.W. Gibson, J. Runt, R.H. Colby, Polymerized ionic liquids with enhanced static dielectric constants, Macromolecules. 46 (2013) 1175–1186. https://doi.org/10.1021/ma301833j.

[27] M. Wübbenhorst, J. Van Turnhout, Analysis of complex dielectric spectra. I: One-dimensional derivative techniques and three-dimensional modelling, in: J. Non. Cryst. Solids, North-Holland, 2002: pp. 40–49. https://doi.org/10.1016/S0022-3093(02)01086-4.

[28] A. Garcia-Bernabé, V. Compañ, M.I. Burguete, E. García-Verdugo, N. Karbass, S. V. Luis, E. Riande, Conductivity and polarization proesses in highly cross-linked supported ionic liquid-like phases, J. Phys. Chem. C. 114 (2010) 7030–7037. https://doi.org/10.1021/jp910535z.

[29] P. Colomban, J.C. Badot, Radiowave and microwave frequency dielectric relaxations at the superionic, incommensurate and ferroelectric phase transitions in NH 4 HSeO 4 and ND 4 DSeO 4, J. Phys. Condens. Matter. 4 (1992) 5625–5638. https://doi.org/10.1088/0953-8984/4/25/016.

[30] A. Eisenberg, M. King, Ion-Containing Polymers: Physical Properties and Structure, in: Academic Press, 1977. https://doi.org/https://doi.org/10.1016/B978-0-12-235050-

4.50007-1.

[31] Y. Zhang, Electronegativities of Elements in Valence States and Their Applications. 2. A Scale for Strengths of Lewis Acids, Inorg. Chem. 21 (1982) 3889–3893. https://doi.org/10.1021/ic00141a006.

[32] M.G. McLin, C.A. Angell, Frequency-dependent conductivity, relaxation times, and the conductivity/viscosity coupling problem, in polymer-electrolyte solutions: LiClO4 and NaCF3SO3 in PPO 4000, Solid State Ionics. 53–56 (1992) 1027–1036. https://doi.org/10.1016/0167-2738(92)90286-X.

[33] D. Fragiadakis, S. Dou, R.H. Colby, J. Runt, Molecular mobility and Li+ conduction in polyester copolymer ionomers based on poly(ethylene oxide), J. Chem. Phys. 130 (2009) 064907. https://doi.org/10.1063/1.3063659.

[34] J. Thomas, Solid state electrochemistry. Edited by PeterG. Bruce, Cambridge University Press, Cambridge 1995, XVI, 344 pp., hardcover, £60.00, ISBN 0-521-40007-4, Adv. Mater. 8 (1996) 360–360. https://doi.org/10.1002/adma.19960080417.

[35] A. Serghei, M. Tress, J.R. Sangoro, F. Kremer, Electrode polarization and charge transport at solid interfaces, Phys. Rev. B - Condens. Matter Mater. Phys. 80 (2009) 184301. https://doi.org/10.1103/PhysRevB.80.184301.

Images

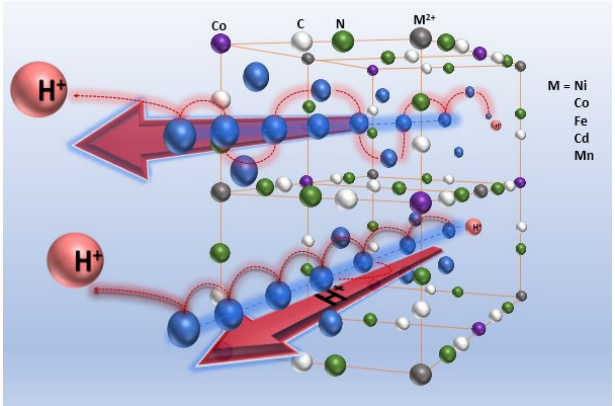

Graphical abstract

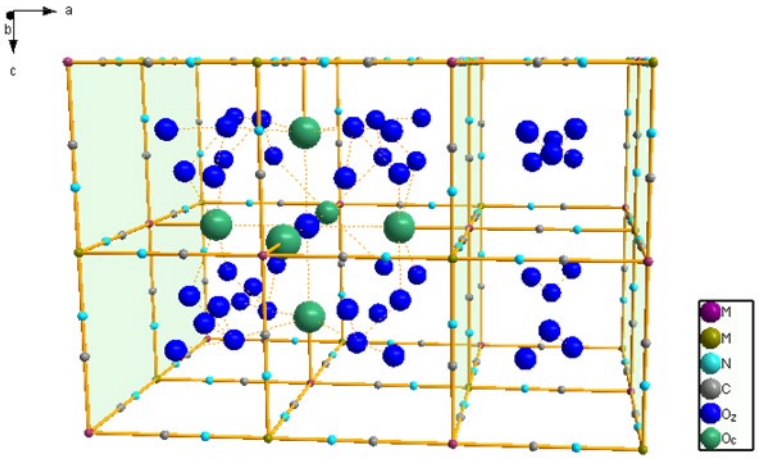

Figure 1. Framework for the $M_3[Co(CN)_6]_2 \cdot xH_2O$ series for the members that crystalize within a Fm-3m space group (random vacancy distribution). Indicated are the coordinated and hydrogen bonded water molecules. Neighboring cavities remain communicated by a network of sambals tunnels formed by the finite –CN– bond length.

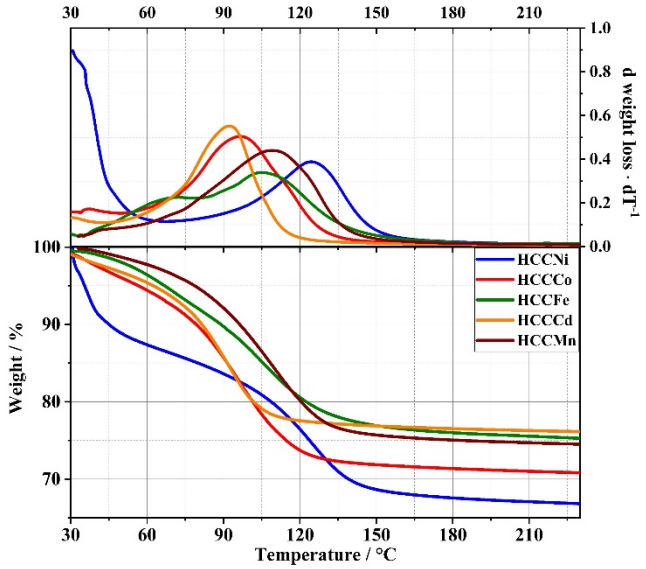

Figure 2. Thermogram (down) and derivate (upper) of the HCCMs samples.

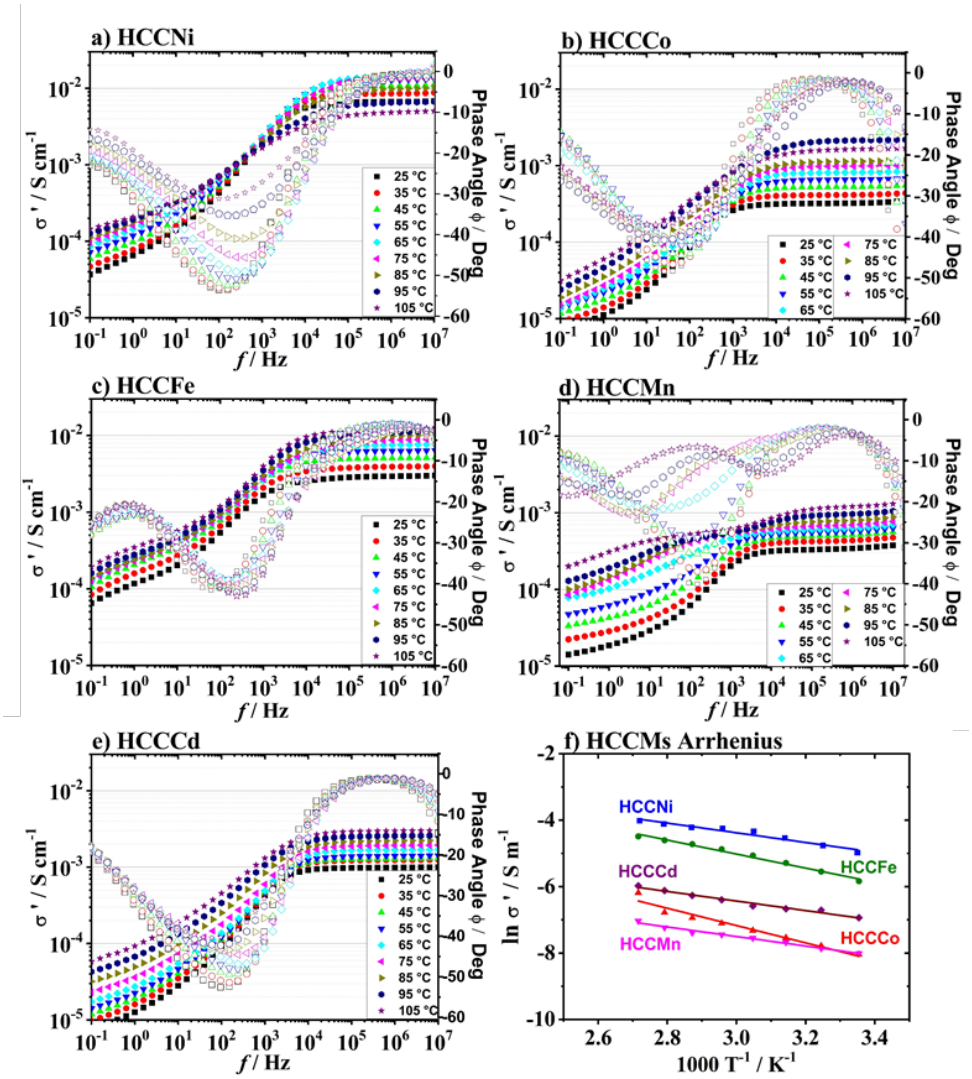

Figure 3. Bode diagrams for the samples: a) HCCNi, b) HCCCo, c) HCCFe, d) HCCMn, e) HCCCd and f) Arrhenius plot for the conductivity of the HCCMs showed in plots a, b, c, d and e.

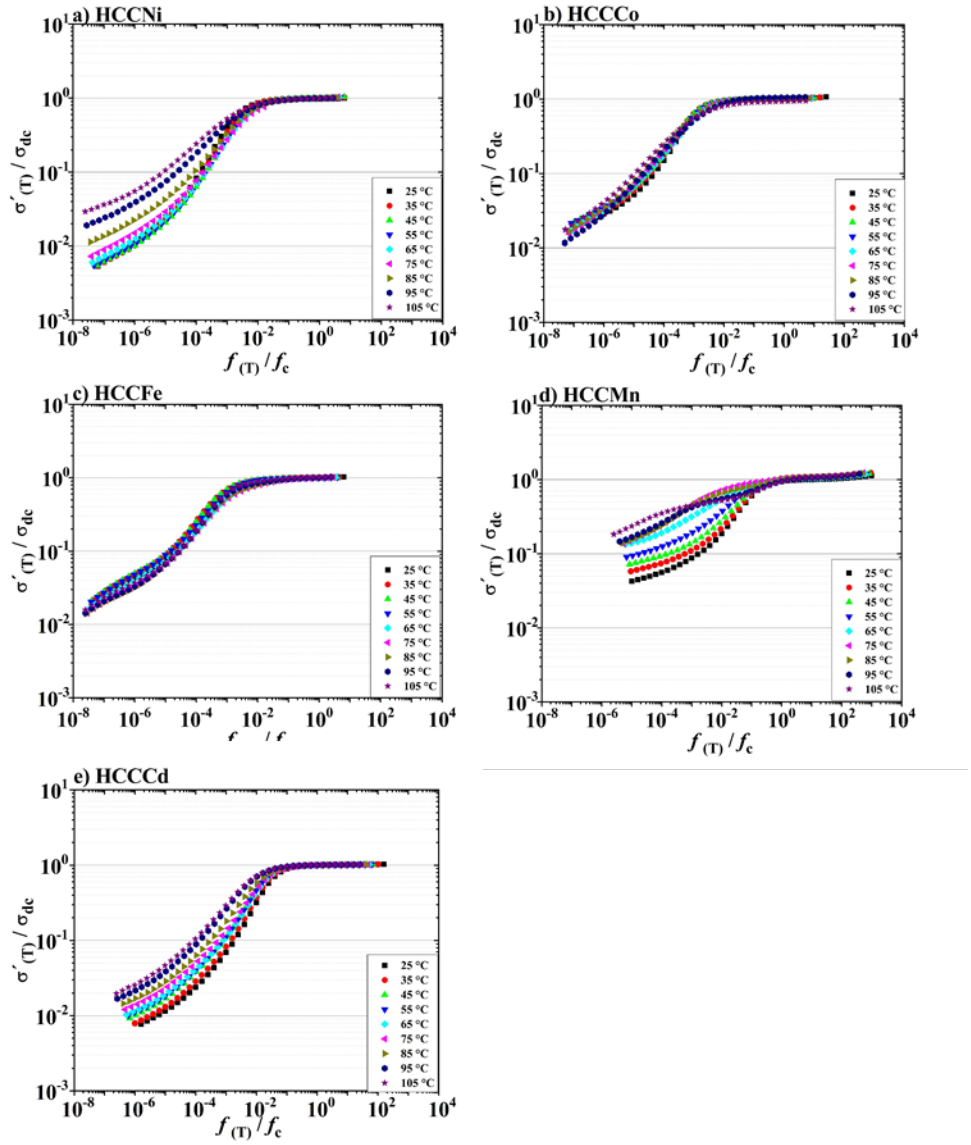

Figure 4. Scaling curves of conductivity in the whole range of temperatures for the samples HCCNi, HCCCo, HCCFe, HCCMn and HCCCd.

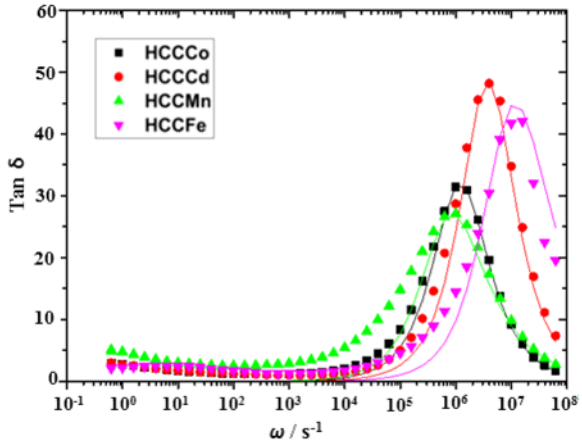

Figure 5. Tan δ as a function of the frequency at 65 ºC for HCCCo, HCCCd, HCCMn and HCCFe. The solid lines indicate the convolution of Eq. (2) in the peak of tan δ at higher frequencies.

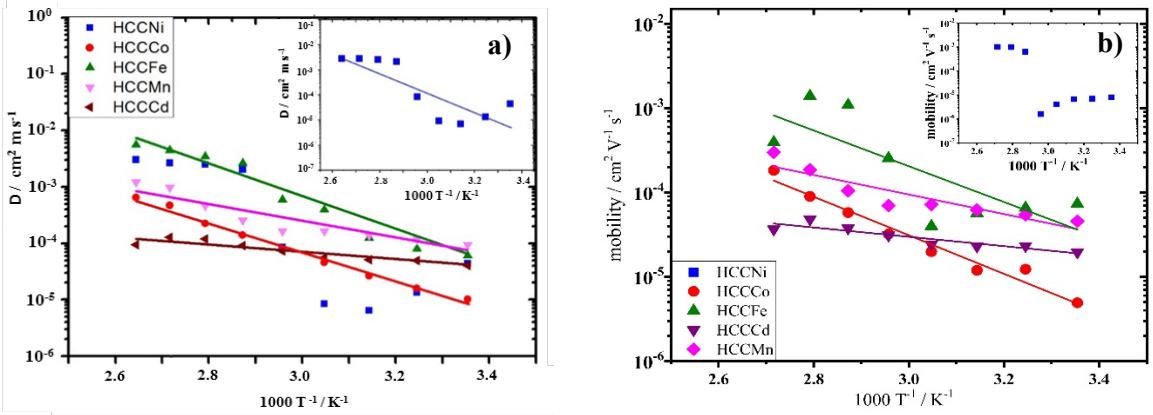

Figure 6. Arrhenius diagram to a) diffusion coefficient and b) charge mobility, obtained from Cole-Cole model.

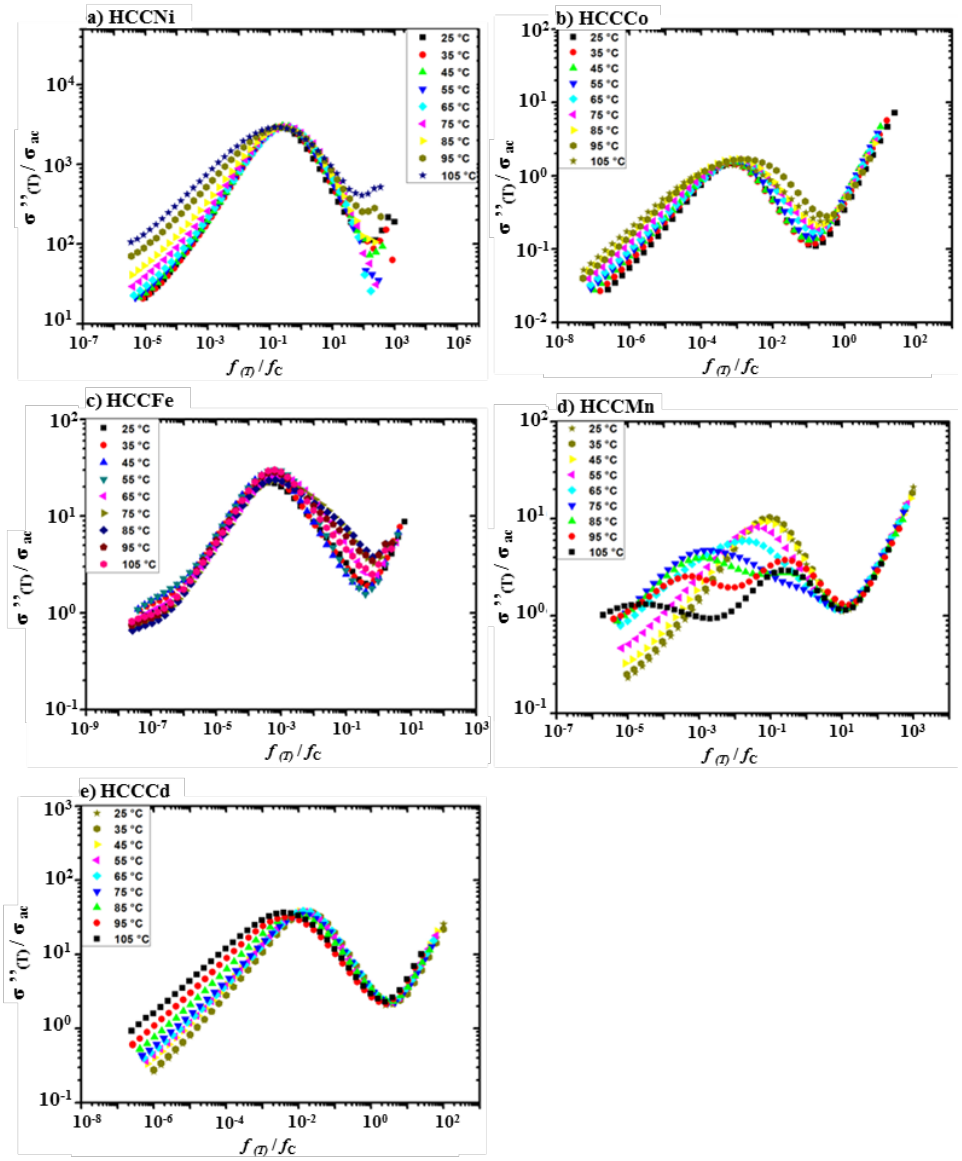

Figure 7. Master curve of the normalized plots respect to the imaginary part of the conductivity for the samples plotted in figure 4S